Neural Multi-Atlas Label Fusion: Application to Cardiac MR Images

Heran Yang[a], Jian Sun[a,*], Huibin Li[a], Lisheng Wang[b], Zongben Xu[a]

[a] *School of Mathematics and Statistics, Xi'an Jiaotong University, China*
[b] *Department of Automation, Shanghai Jiaotong University, China*

Abstract

Multi-atlas segmentation approach is one of the most widely-used image segmentation techniques in biomedical applications. There are two major challenges in this category of methods, *i.e.*, atlas selection and label fusion. In this paper, we propose a novel multi-atlas segmentation method that formulates multi-atlas segmentation in a deep learning framework for better solving these challenges. The proposed method, dubbed deep fusion net (DFN), is a deep architecture that integrates a feature extraction subnet and a non-local patch-based label fusion (NL-PLF) subnet in a single network. The network parameters are learned by end-to-end training strategy for automatically learning deep features that enable optimal performance in a NL-PLF framework. Besides, the learned deep features are further utilized in defining a similarity measure for atlas selection. We evaluate our proposed method on two public cardiac MR databases of SATA-13 and LV-09 for left ventricle segmentation, and our learned DFNs with extracted deep features for atlas selection at testing phase achieve state-of-the-art accuracies, *e.g.*, 0.833 in averaged Dice metric (ADM) on SATA-13 database and 0.95 in ADM for epicardium segmentation on LV-09 database. Besides, our method is robust to the cross-database evaluation, *e.g.*, the DFN learned on LV-09 database achieves 0.815 in ADM on SATA-13 database. We also test our proposed method on Cardiac Atlas Project (CAP) testing set of MICCAI 2013 SATA Segmentation Challenge, and our method achieves 0.815 in Dice metric, ranking as the highest result on this dataset.

Keywords: Multi-atlas label fusion, left ventricle segmentation, deep learning, atlas selection.

1. Introduction

As one of the most successful medical image segmentation techniques over the past decade, multi-atlas segmentation (MAS) has been applied to the segmentation of a variety of medical images, including abdominal (Tong et al.,

*Corresponding author
Email address: jiansun@mail.xjtu.edu.cn (Jian Sun)

2015; Wang et al., 2014; Wolz et al., 2013; Xu et al., 2015), cardiac (Xie et al., 2015; Bai et al., 2015, 2013; Zhuang and Shen, 2016; Isgum et al., 2009; Pouch et al., 2014) and brain images (Wu et al., 2014; Asman and Landman, 2013; Coupé et al., 2011; Duc et al., 2013; Artaechevarria et al., 2009; Sanroma et al., 2014; Wang et al., 2013; Cardoso et al., 2013; Asman et al., 2015).

Given an image to be segmented, *i.e.*, a *target image*, multi-atlas segmentation methods utilize multiple images from different subjects with manual segmentation labels to estimate segmentation of the target image, *i.e.*, *target labels*. Here, a group of images from the same subject with segmentation masks labeled by experts is called an atlas. Typically, a multi-atlas segmentation method first registers atlas images to the target image, and then the corresponding warped atlas labels are combined to estimate the target label by a label fusion procedure (Iglesias and Sabuncu, 2015). To raise computational efficiency or improve final segmentation accuracy, multi-atlas segmentation methods employ an atlas selection procedure to select a few warped atlas images most similar to the target image, and only the labels of these selected images are utilized in the label fusion procedure (Aljabar et al., 2009).

A large body of literatures on multi-atlas segmentation focus on the label fusion procedure. One typical label fusion strategy is weighted voting, where the label of each target voxel is determined by weighted average of the labels of corresponding voxels in warped atlas images. *Local label fusion* methods determine the voxel-wise fusion weights by local intensity-based similarities between the target and atlas voxels (Artaechevarria et al., 2009; Makropoulos et al., 2014). To account for possible registration errors, Coupé et al. (2011) firstly considered all voxels in a search window or volume around the registered atlas voxel when predicting the label of a target voxel. Because the fusion weights are defined as the intensity similarities between image patches respectively centered at the target and atlas voxels, this category of methods (Bai et al., 2015; Iglesias and Sabuncu, 2015; Wang et al., 2014) is commonly named as *non-local patch-based label fusion*. To the best of our knowledge, it has been the state of the art in multi-atlas segmentation before the emergence of deep learning approach. Moreover, statistical fusion methods were proposed to estimate the fusion weights by integrating models of rater performance (Cardoso et al., 2013; Asman and Landman, 2013; Warfield et al., 2004). Instead of using weighted voting strategy, sparsity-based dictionary learning (Tong et al., 2015) and matrix completion (Sanroma et al., 2015) methods were also proposed to predict the target labels by representing image and label patch pairs with sparse regularization or low rank constraint.

Atlas selection, another important issue in multi-atlas segmentation, aims at selecting the most relevant atlases, which is generally achieved by ranking the atlases according to their similarities to the target image, for better predicting the target labels. The traditional methods rank atlases by using intensity-based similarity measures, *e.g.*, normalized mutual information (Studholme et al., 1999; Collignon et al., 1995). Other well-designed measures for atlas selection include the distance between transformations (Commowick et al., 2009), registration consistency (Heckemann et al., 2009), *etc.* Machine learning methods were also

introduced to learn similarity measures for atlas selection, *e.g.*, manifold learning (Duc et al., 2013), ranking SVM (Sanroma et al., 2014), *etc.*

Deep learning approach has been a hot research topic in machine learning and achieved remarkable results in computer vision, natural language processing, *etc.* In recent years, deep learning approach was widely applied in medical image analysis, *e.g.*, vessel segmentation (Fu et al., 2016; Maninis et al., 2016; Khalaf et al., 2016), brain segmentation (Wachinger et al., 2017; Moeskops et al., 2016; Rajchl et al., 2017), *etc.* These methods commonly design different deep network structures considering distinct features of specific problems, and directly learn the optimal network parameters for voxel-wise label prediction. For example, Havaei et al. (2017) proposed two-pathway cascaded deep networks with a two-phase training procedure for brain tumor segmentation. Chen et al. (2017) designed a multi-task fully convolutional network with multi-level contextual information for object instance segmentation from histology images. Moreover, Kamnitsas et al. (2017) designed an 11-layers multi-scale 3D convolutional neural network with two convolutional pathways for lesion segmentation in multi-modal brain MRI. Due to the possible reasons, such as the lack of incorporating global shape constraints into the network, insufficient labeled training data, or suboptimal optimization of network parameters, *etc.*, using deep networks alone may not lead to satisfactory results. Therefore, some methods utilize deep networks to achieve preliminary segmentation masks and then refine them by some post-processing procedures, *e.g.* level set method (Avendi et al., 2016; Ngo et al., 2017) or deformable model (Guo et al., 2016), in order to impose global shape constraints on the network outputs.

In this paper, we propose a novel multi-atlas segmentation method by reformulating the non-local patch-based label fusion (NL-PLF) method (Coupé et al., 2011; Bai et al., 2015) to be a deep neural network (Krizhevsky et al., 2012). On the one hand, non-local patch-based label fusion is an effective approach for multi-atlas segmentation, but relies on handcrafted features for computing the label fusion weights. For example, for a given voxel in the image, Coupé et al. (2011) used the voxel intensities in a image patch centered at this voxel as its features, while Bai et al. (2015) incorporated the image intensities and gradient orientations of all voxels within a image patch centered at this voxel and the context difference of this image patch with regard to its surrounding patches into the features of this voxel. These handcrafted features have been justified to be effective but may not be optimal for label fusion. Taking advantage of strong feature learning ability of deep learning approach, we integrate the modules of feature learning and label fusion into a trainable deep architecture, and learn optimal image features for label fusion in multi-atlas segmentation framework. On the other hand, convolutional neural networks generally predict the voxel-wise segmentation labels by performing classification for each voxel (Vincent et al., 2008; Hinton and Salakhutdinov, 2006), which is hard to incorporate the global shape constraints of anatomical structures or tissues into the framework of deep learning. Therefore, conventional deep learning methods generally rely on post-processing procedures, *e.g.*, deformable model (Guo et al., 2016), to generate a final connected segmentation mask. Different from these approaches, our

proposed multi-atlas segmentation method relies on atlas-to-target registration, which can naturally transfer the shape constraints of anatomical structures to the target image with the help of an accurate inter-subject image registration, and the label fusion procedure only concentrates on fusing these transformed labels, which may potentially reduce the requirement of a large labeled training dataset.

1.1. Contributions

The main contributions of our approach can be summarized as follows:

1) We propose a novel deep architecture for multi-atlas segmentation, which comprises a feature extraction subnet for extracting deep features, and a non-local patch-based label fusion subnet for fusing the warped atlases, as shown in Fig. 1. To the best of our knowledge, this is the first work to accomplish the conventional label-fusion-based multi-atlas segmentation method in a deep learning framework.
2) Deep fusion net can discriminatively learn the optimal deep features for fusion weights computation by an end-to-end training process, compared with the handcrafted features utilized in traditional multi-atlas segmentation methods.
3) Deep fusion net naturally defines a similarity measure for atlas selection at patch level, shown to be especially effective with inaccurate registration in experimental section.
4) Deep fusion net achieves state-of-the-art accuracies for LV segmentation on two publicly available cardiac MR databases, *i.e.*, MICCAI 2013 SATA Segmentation Challenge (SATA-13) database [1] and MICCAI 2009 LV Segmentation Challenge (LV-09) database [2] (Radau et al., 2009).

Note that a preliminary version of this work was presented in Yang et al. (2016). Compared with the conference paper, the current paper presents the following contributions. (1) We presented additional discussions on the details and insights of the proposed method for better readability; (2) Our method was evaluated on additional dataset (LV-09 database) and compared with more segmentation methods; (3) More experiments were conducted to further explore the behaviors of the proposed method, *e.g.*, impact of atlas selection strategy, cross-database evaluation, *etc.*

1.2. Related work on left ventricle segmentation

The proposed deep fusion net is applied to left ventricle (LV) segmentation from short axis cardiac MR images (Petitjean and Dacher, 2011), and we therefore review the related work on LV segmentation. Accurately segmenting the LV from cardiac MR images is essentially important for quantitatively assessing the cardiac function in clinical diagnosis, which is still a challenging task due to

[1] https://masi.vuse.vanderbilt.edu/workshop2013/index.php
[2] https://smial.sri.utoronto.ca/LV_Challenge/Home.html

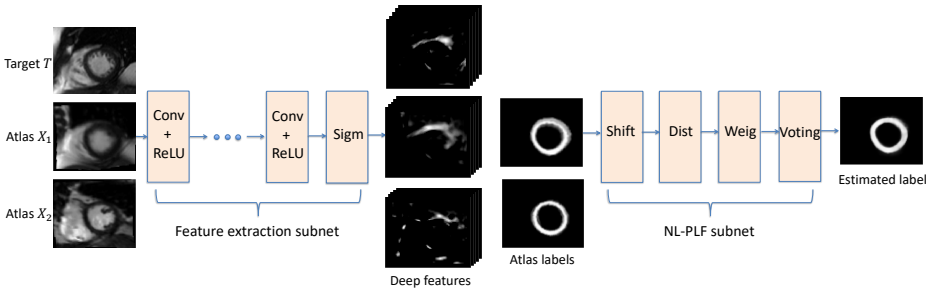

Fig. 1: The architecture of deep fusion net. A target image T and its warped atlas images X_i are first fed into a *feature extraction subnet* to extract deep features. These features and atlas labels are then sent to a *non-local patch-based label fusion (NL-PLF) subnet* for generating the estimated label of target image, *i.e.*, target label.

large variation of LV in intensity levels or structural shapes, respiratory motion artifacts, partial volume effects, *etc.*

As an effective approach for LV segmentation, multi-atlas segmentation methods generally register atlas images to the target image, and then fuse the warped atlas labels by computing the fusion weights, which are generally defined by intensity-based similarities. For example, Bai et al. (2015) incorporated the intensity, gradient and contextual information into an augmented feature vector for similarity measure in the non-local patch-based label fusion framework. Instead of only considering the corresponding atlas slice to the target image, Xie et al. (2015) fused the labels of all atlas slices in a neighborhood to produce a more accurate estimated target label. Most of these methods utilize the handcrafted features for computing the label fusion weights. These features are designed by human experiences and hard to be guaranteed in optimality. Moreover, some methods estimate the target label by statistical theory. For example, considering that different atlases may produce similar label errors, Wang et al. (2013) formulated the weighted voting as minimizing total expectation of labeling error and pairwise dependency between atlases was modeled as the joint probability of two atlases making a segmentation error at a voxel. Due to the close connection between label fusion and registration, Bai et al. (2013) attempted to alternately perform patch-based label fusion and registration refinement. For a comprehensive review on multi-atlas segmentation, please refer to Iglesias and Sabuncu (2015).

In recent years, deep learning approach was also applied to LV segmentation. For example, Avendi et al. (2016) utilized convolutional neural networks to determine the region of interests (ROI) containing LV and stacked autoencoders to infer the LV segmentation mask. Then the segmentation mask was incorporated into level set model to produce the final segmentation result. Similarly, Ngo et al. (2017) first estimated the ROI and an initial segmentation by deep belief network and Otsu's thresholding, and then refined the initial segmentation by level set model. Both of these two approaches achieve high accuracies on MICCAI 2009 LV Segmentation Challenge database, but their performance

largely relies on the post-processing method, *i.e.* level set model.

Compared with the related work above, our method bridges the multi-atlas segmentation method and deep learning method. Contrary to the conventional label fusion using handcrafted features, our method learns discriminative features for label fusion. Contrary to the current deep learning segmentation methods, which learn a mapping directly from the image intensity space to the label space, our net is a label fusion net relying on the registration of atlas to target image. Specifically, we learn deep features to compute optimal fusion weights for fusing the warped atlas labels provided by registration, which reduces the ambiguities in classification purely based on local intensities.

2. Deep fusion net for multi-atlas segmentation

We now present our proposed deep fusion net for multi-atlas segmentation, including the network architecture, its training and testing procedures.

2.1. General framework

In multi-atlas segmentation, multiple atlas images are first registered to the target image by non-rigid registration, and then the corresponding atlas labels are warped to the target image using these transformations. Our deep fusion net is designed to fuse the warped atlas labels using discriminatively learned deep features to estimate an accurate label map for the target image.

As shown in Fig. 1, deep fusion net (DFN) for multi-atlas segmentation is defined as a feature extraction subnet, followed by a non-local patch-based label fusion (NL-PLF) subnet. The first subnet is responsible for extracting dense features from target and atlas images, and the second one aims at fusing the warped atlas labels using these extracted features. This net integrates the modules of feature extraction and label fusion in a trainable deep architecture.

Assume that a target image T and a number of atlases are given. After registering the atlas images to the target image T, the warped atlas image and label pairs are denoted as $\{X_i, L(X_i)\}_{i=1}^{K}$, where K is the number of atlases. The computation of the estimated target label by deep fusion net can be divided into two parts. *First*, the target image T and warped atlas images $\{X_i\}_{i=1}^{K}$ are fed into feature extraction subnet to output their per-pixel features $F(T)$ and $\{F(X_i)\}_{i=1}^{K}$. *Then*, these extracted features and warped atlas labels $\{L(X_i)\}_{i=1}^{K}$ are fed into NL-PLF subnet to generate the estimated target label. The network parameters are learned by an end-to-end training process, which is based on a loss defined between network output and ground-truth target label.

In the following sections 2.2 and 2.3, we will respectively introduce the feature extraction subnet and NL-PLF subnet in detail.

2.2. Feature extraction subnet

The feature extraction subnet aims at extracting the deep features representing the image patches as a manifold, on which the distance of deep features is a meaningful image similarity measure. This is enforced by the fact that this

subnet tries to support the minimization of segmentation loss via the follow-up NL-PLF subnet. Note that all input images of this subnet, including the target image and warped atlas images, share the same subnet parameters, i.e., only one feature extraction subnet is learned for all images.

As shown in Fig. 1, the feature extraction subnet consists of multiple repetitions of convolutional layer with ReLU activation function, and a final sigmoid layer for feature normalization.

2.2.1. Convolutional layer

The convolutional layer, which aims to learn discriminative local patterns represented by filters from its input features, is the core building block of convolutional neural network (CNN). This layer convolves the input features using a set of learnable filters $\{\mathcal{W}_{d'}\}_{d'=1}^{D'}$, and each filter $\mathcal{W}_{d'} \in \mathbb{R}^{w_f \times w_f \times D}$ is a third-order tensor, where D' is the number of filters, D denotes the number of *feature maps* in input features, and $w_f \times w_f$ is the receptive field of filters.

Given the input features $G^{l-1}(X) \in \mathbb{R}^{M \times N \times D}$ of image X, the $l-$th convolutional layer outputs features $G^{l}(X) \in \mathbb{R}^{(M-w_f+1)\times(N-w_f+1)\times D'}$, whose d'-th feature map, denoted as $g_{d'}^{l}$, can be written as

$$g_{d'}^{l} = \varphi\left(W_{d'} * G^{l-1}(X) + b_{d'}^{l}\right), \tag{1}$$

where $*$ is the 3-D convolution operator, and $b_{d'}^{l}$ is the bias term. φ is a rectified linear unit (ReLU) function (Krizhevsky et al., 2012) that is defined as $\varphi(x) = \max(0, x)$.

2.2.2. Sigmoid layer

The sigmoid layer is defined to normalize the extracted features for robustly computing feature distances in NL-PLF subnet. Given input features $G(X) \in \mathbb{R}^{M \times N \times D}$ of image X, each element $f_{m,n,d}$ in the normalized features $F(X) \in \mathbb{R}^{M \times N \times D}$ can be computed by processing each element $g_{m,n,d}$ of $G(X)$ by

$$f_{m,n,d} = \frac{1}{1 + e^{-g_{m,n,d}}}, \tag{2}$$

where (m, n, d) denotes the three-dimensional index of element in input or normalized features.

2.3. Non-local patch-based label fusion subnet

This subnet is a deep architecture implementing non-local patch-based label fusion scheme on top of feature extraction subnet. As shown in Fig.1, our NL-PLF subnet consists of *shift layer, distance layer, weight layer* and *voting layer*, and finally outputs the estimated label of target image.

Figure 2(a) shows the idea of non-local patch-based label fusion scheme. For simplicity, we use the notation p to denote pixel position instead of (m, n). To account for atlas-to-target image registration errors, all the pixels in a search window around the pixel p in warped atlas images $\{X_i\}_{i=1}^{K}$ are considered as the

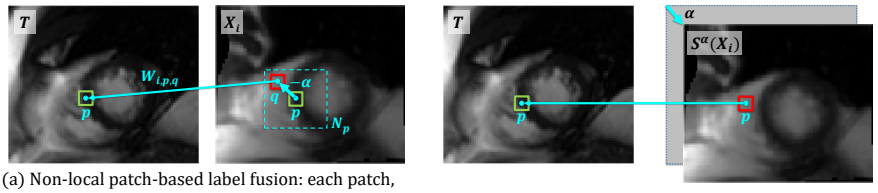

(a) Non-local patch-based label fusion: each patch, e.g., patch around q, in a window N_p around p votes for the label of pixel p in T.

(b) Shift operation: feature distance between p of T and q of X_i in (a) equals to feature distance of T and $S^\alpha(X_i)$ at p.

Fig. 2: Illustration of non-local patch-based label fusion and shift operation.

potential corresponding pixels for the pixel p in target image T. Therefore, the labels of these pixels in atlas images are fused to produce the estimated target label at pixel p.

Contrary to the handcrafted features adopted in Bai et al. (2015), deep fusion net computes the fusion weights using the deep features extracted by the feature extraction subnet. The fusion weights are defined as the normalized distances between these deep features, and the normalization is accomplished by softmax operator, enforcing that the summation of all fusion weights related to each pixel p in target image T is one. More precisely, the fusion weight of pixel q in warped atlas image X_i for predicting the label of pixel p in target image T is determined as

$$w_{i,p,q}(\Theta) = \frac{\exp(-||F_p(T;\Theta) - F_q(X_i;\Theta)||_2^2)}{\sum_j \sum_{q' \in N_p} \exp(-||F_p(T;\Theta) - F_{q'}(X_j;\Theta)||_2^2)}, \tag{3}$$

where Θ is the network parameters, *i.e.*, filters and biases, in feature extraction subnet. $F_p(T;\Theta)$ is the extracted feature vector of image T at pixel p, and N_p is the search window around pixel p.

Hence, the estimated label of pixel p in target image T can be written as

$$\hat{L}_p(T;\Theta) = \sum_i \sum_{q \in N_p} w_{i,p,q}(\Theta) L_q(X_i), \tag{4}$$

where $L_q(X_i)$ is the label of atlas image X_i at pixel q.

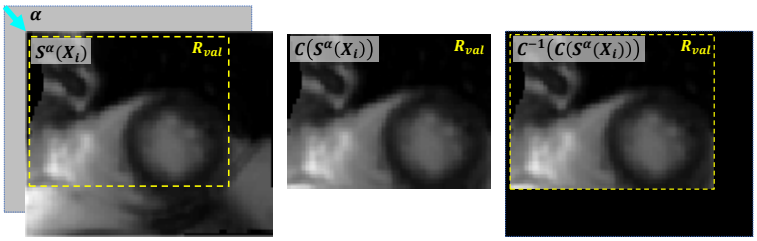

Fig. 3: Illustration of cropping operation C on shifted atlas image $S^\alpha(X_i)$. Left to right: shifted atlas image $S^\alpha(X_i)$, cropped region by operation C, and the result of applying inverse cropping operation C^{-1} to the cropped region. The yellow dashed box denotes valid set R_{val}.

The objective of learning deep fusion net is to enforce that the estimated label of target image T in Eqn.(4) should approximate the ground-truth target label $L(T)$ as close as possible. Therefore, we define a *loss layer* to measure the approximation error:

$$E(\hat{L}(T;\Theta), L(T)) = \frac{1}{P}\left\|\hat{L}(T;\Theta) - L(T)\right\|_F^2 , \tag{5}$$

where $\|\cdot\|_F$ is the Frobenius norm and P denotes the number of pixels in target image T. Our task in network training is to minimize this loss function on a training set *w.r.t.* the network parameters Θ using back-propagation. For notational convenience, we will omit the network parameters Θ in the rest of the paper.

As shown in Eqn.(3), the computations of fusion weights are highly non-linear and depend on the pairwise feature distances within search window, leading to difficulties of fast calculating the fusion weights and their gradients in deep networks. Therefore, we decompose the computations of the fusion weights into several successive simple operations, modeled as *shift layer*, *distance layer* and *weight layer*. Each operation and the gradient of its output *w.r.t.* input can be easily calculated using GPU during network training.

Figure 2 shows our motivation for this decomposition in detail. Instead of directly computing the feature distance of pixel p in target image T and pixel q in atlas image X_i, shown in Fig. 2(a), we can equivalently compute the per-pixel feature distance at the pixel p between target image T and the shifted atlas image X_i by the shift vector $\alpha = p - q$, as shown in Fig. 2(b).

Suppose that the search window width is $2t+1$. To fast calculate the fusion weights using Eqn.(3) in deep networks, we first shift each feature map of X_i by each shift vector α within the non-local region $R_{nl} = \left\{(u,v) \in \mathbb{Z}^2 | -t \leq u, v \leq t\right\}$ using a *shift layer*, then compute the pixel-wise feature distances using a *distance layer*, and finally transform these distances into fusion weights using a *weight layer*.

2.3.1. Shift layer

The shift layer spatially shifts the extracted features or label map of each atlas image. Given the extracted features $F(X_i) \in \mathbb{R}^{M\times N\times D}$ of atlas image X_i, this layer generates $(2t+1)\times(2t+1)$ spatially shifted features along each shift vector $\alpha \in R_{nl}$. Due to the boundary effect, we remove the boundary and only retain features of pixels within the spatially valid set: $R_{val} = \left\{(m,n) \in \mathbb{Z}^2 | t < m \leq M-t, t < n \leq N-t\right\}$.

Each output of the shift layer can be written as $C(S^\alpha(F(X_i)))$, where S^α denotes the shift operator with a shift vector α, and C denotes the cropping operation. Figure 3 illustrates an example of cropping operation C on shifted atlas image $S^\alpha(X_i)$. Since the operation C has no effect on the pixels within the valid set R_{val}, the output $C(S^\alpha(F(X_i)))$ at any pixel $p \in R_{val}$ can be formulated as

$$[C(S^\alpha(F(X_i)))]_p = [S^\alpha(F(X_i))]_p = [F(X_i)]_q , \tag{6}$$

where $q = p - \alpha$ and $[\cdot]_p$ denotes the feature vector at pixel p.

The gradient of network loss E in Eqn.(5) *w.r.t.* the input feature $F(X_i)$ can be calculated as

$$\frac{\partial E}{\partial F(X_i)} = \sum_{\alpha \in R_{nl}} S^{-\alpha} \left(C^{-1} \Big(\frac{\partial E}{\partial C(S^{\alpha}(F(X_i)))} \Big) \right), \tag{7}$$

where $\frac{\partial E}{\partial C(S^{\alpha}(F(X_i)))}$ is the gradient of network loss E *w.r.t.* the output of this shift layer, *i.e.*, $C(S^{\alpha}(F(X_i)))$. C^{-1} denotes the inverse operation of C, which adds the removed boundary to the cropped region by constant zero, as shown in Fig. 3.

2.3.2. Distance layer

The distance layer computes the pixel-wise feature distance at each pixel p between the shifted features $S^{\alpha}(F(X_i))$ of atlas X_i and the target's features $F(T)$ within R_{val} as

$$D_p^{\alpha}(T, X_i) = \left\| [C(S^{\alpha}(F(X_i)))]_p - [C(F(T))]_p \right\|_2^2 . \tag{8}$$

It is defined as the pixel-wise L_2 distance, and the gradient of this layer can be simply derived *w.r.t.* both $C(S^{\alpha}(F(X_i)))$ and $C(F(T))$. As mentioned in section 2.3.1, the cropping operation C can be ignored within R_{val}.

2.3.3. Weight layer

The weight layer maps the feature distances to fusion weights using softmax operation. The fusion weight of pixel q ($q = p - \alpha, \alpha \in R_{nl}$) in atlas image X_i for predicting the label of pixel p in target image T can be written as

$$w_{i,p,q} = w_p^{\alpha}(X_i) = \frac{e^{-D_p^{\alpha}(T, X_i)}}{\sum_j \sum_{\alpha' \in R_{nl}} e^{-D_p^{\alpha'}(T, X_j)}} . \tag{9}$$

This softmax operation is a common layer in architecture of deep networks, and the gradient of this layer *w.r.t.* the input $D_p^{\alpha}(T, X_k)$ can be easily derived (Goodfellow et al., 2016), where k is any atlas index.

2.3.4. Voting layer

The voting layer estimates the label of target image T at pixel p by

$$\hat{L}_p(T) = \sum_i \sum_{\alpha \in R_{nl}} w_p^{\alpha}(X_i) [C(S^{\alpha}(L(X_i)))]_p \ , p \in R_{val}. \tag{10}$$

As a linear operation, the gradient of this layer can also be easily derived *w.r.t.* the input $w_p^{\alpha}(X_i)$.

Summary: The non-local patch-based label fusion subnet successively processes the extracted features and warped atlas labels by *shift*, *distance*, and *weight layers* to output fusion weights, which are then utilized by *voting layer* to estimate the target label. This subnet implements Eqn.(3) by using the above simple layers, and the gradients of these layer can be easily computed using GPU in network training.

2.4. Network training

We learn the network parameters Θ by minimizing the loss in Eqn.(5) *w.r.t.* Θ using back-propagation.

Given a number of atlases for training, each atlas is selected as the target image in turn, and then the remaining atlases are registered to this target image as the warped atlases. Suppose that i-th atlas is picked as the target image T with ground-truth label $L(T)$, the corresponding warped atlases are denoted by $\mathcal{A}_i = \{X_j, L(X_j)|j = 1, 2, ..., K, j \neq i\}$, where K is the total number of atlases.

We use stochastic gradient descent in training, and each triplet of $(\mathcal{A}_i, T, L(T))$ is taken as a batch. Instead of using all warped atlases within $\mathcal{A}_i$ in each batch, which may require a large GPU memory and long training time, we randomly sample K_0 ($K_0 = 5$) warped atlases for training, according to a distribution proportional to the normalized mutual information between warped atlas images $\{X_j|j = 1, 2, ..., K, j \neq i\}$ and the target image T. This random selection strategy enriches the diversity of warped atlases for target image in the training phase. Since there may be discrepancy between distributions of training and testing data, this strategy may improve the generalization ability of deep fusion net for testing data. We will evaluate the atlas selection strategy at training phase in section 3.5. Many randomized techniques were also proposed in deep learning to improve network generalization ability, *e.g.*, dropout (Srivastava et al., 2014), data augmentation (Vincent et al., 2008), *etc.*

In current experimental setup, the GPU memory requirement for processing one target image is about $O\big(MNDK_0(2t+1)^2\big)$. In practice, for a deep fusion net with network parameters in section 3.3, one forward-backward process takes about 4GB GPU memory for a target image in size of 120×140 with $K_0 = 5$. The GPU requirement is linear *w.r.t.* the number K_0, and the sensitivity of network performance *w.r.t.* K_0 will be discussed in section 3.5.

2.5. Network testing

In the testing phase, the learned deep fusion net loads a test sample (a target image and its warped atlases) and outputs the estimated target label. To improve the accuracy, we only pick a few most similar atlases for the target image. As discussed in section 2.2, feature extraction subnet actually learns an embedding space at training process, in which pixel-wise L_2 distance within distance layer corresponds to image similarity, *i.e.*, similar pixels have small distances and distinct ones have large distances. Therefore, we can naturally define a deep feature distance between a target image T and its warped atlas image X_i as

$$d_F(T, X_i) = \big\|F(T) - F(X_i)\big\|_F^2 , \tag{11}$$

where $F(\cdot)$ is the extracted features using well-trained feature extraction subnet at training process. We take the top-k atlases with smallest deep feature distances as the selected atlases for a target image, which are then fed into the learned deep fusion net to estimate the target label. Notably, the number of selected atlases at testing process does not need to be same as K_0 used in the training phase, whose sensitivity will be further explored in section 3.5.

3. Experiments

In this section, we evaluate the performance of our deep fusion net on two cardiac MR datasets for left ventricle (LV) segmentation. In the following paragraphs, we will compare our method with other segmentation methods and further explore the behaviors of our proposed method on these two databases.

3.1. Databases

3.1.1. SATA-13 database

The MICCAI 2013 SATA Segmentation Challenge provides a cardiac dataset for LV segmentation. The samples in this dataset are randomly selected from the DETERMINE (Defibrillators to Reduce Risk by Magnetic Resonance Imaging Evaluation) in Cardiac Atlas Project (CAP). The cardiac MR images are acquired using the steady-state free precession (SSFP) pulse sequence, and each image is acquired during a breath-hold of 8-15 seconds duration. Sufficient short-axis slices are obtained to cover the whole heart, and the MR parameters vary between cases. Typically, each cine image sequence has about 25 frames, and each frame has about 10 slices. The size of slice ranges from 138×192 to 512×512. The slice thickness is less than 10 mm, and the gap between slices is less than 2 mm.

The SATA-13 database includes 83 training subjects and 72 testing subjects, and only the ground-truth segmentations of training subjects are provided. We evaluate our deep fusion net on end-diastole (ED) frame of 83 training subjects using 5-fold cross validation, *i.e.*, one fifth of training subjects are taken as validation set and the remaining four fifths of subjects are taken for learning deep fusion net in each fold. The 3D Dice metric (DM) and 3D Hausdorff distance (HD) averaged over the validation sets in five folds are taken as the final accuracies. Assume that Ω_{gt} and Ω_{et} are respectively the ground-truth and estimated segmentations represented by sets of pixels labeled as object of interest, DM and HD between them are defined as $DM(\Omega_{gt}, \Omega_{et}) = \frac{2|\Omega_{gt} \cap \Omega_{et}|}{|\Omega_{gt}|+|\Omega_{et}|}$ and $HD(\Omega_{gt}, \Omega_{et}) = \max\big(\max_{p \in \Omega_{gt}} (\min_{q \in \Omega_{et}} d(p,q)), \max_{q \in \Omega_{et}} (\min_{p \in \Omega_{gt}} d(p,q))\big)$, where $|\cdot|$ denotes the number of elements in a set and $d(p,q)$ denotes the Euclidean distance between coordinates of pixels p and q. The Hausdorff distance is computed in spatial resolution of millimeter obtained from the DICOM file.

3.1.2. LV-09 database

The MICCAI 2009 Cardiac MR LV Segmentation Challenge database (Radau et al., 2009) was recently released to the public. The database is provided by Sunnybrook Health Sciences Centre, and contains 45 subjects with expert annotations, respectively in subsets of "training", "testing" and "online". The cardiac cine-MR short-axis images are acquired using SSFP pulse sequence with a 1.5T GE Signa MRI. All images are obtained during 10-15 second breath-holds with a temporal resolution of 20 cardiac phases over the heart cycle. Each subject contains all slices at end-diastole (ED) and end-systole (ES) frames, and each frame contains 6-12 short axis images obtained from the atrioventricular

ring to the apex (thickness = 8 mm, gap = 8 mm, FOV = 320×320 mm, matrix = 256×256). Both endocardial and epicardial contours are drawn by experienced cardiologists in all slices at ED frame, while only endocardial contours are given at ES frame.

In the experiment, as in Avendi et al. (2016), we utilize 15 training subjects for learning deep fusion net, and 30 subjects in testing and online sets for evaluating the performance. The standard evaluation scheme of MICCAI LV-09 Segmentation Challenge (Radau et al., 2009) is utilized in our comparison, which is based on the following three measures: 1) percentage of "good" contours, 2) the averaged 2D Dice metric (ADM) of the "good" contours, and 3) averaged 2D perpendicular distance (APD) of the "good" contours. A contour is classified as "good" if APD is less than 5 mm.

3.2. Preprocessing

Before starting to learn deep fusion net, atlas images are registered to the target image using ITK software package [3], and we utilize two different registration frameworks to test the robustness of our proposed method.

Landmark-based (LB) registration: Each atlas subject is warped to the target subject using landmark-based registration with 3D affine transformation, and five landmarks are manually labeled at both atlas and target images, as in Bai et al. (2013). These landmarks are also used to crop the region of interests (ROI) from complex backgrounds to reduce the computational cost of registration. To compensate for the potential inter-slice shift, 2D B-spline registration is then utilized on each pair of slices in atlas and target subjects respectively.

Landmark-free (LF) registration: The ROI is cropped by a bounding box on each subject determined by two corner points, and then each atlas subject is warped to the target subject by 3D affine registration without using any landmarks. Normalized mutual information (NMI) is taken as the similarity metric. At last, 2D affine registration and 2D B-spline registration are successively applied to each slice for reducing the potential inter-slice shift.

Generally speaking, LB framework would produce more accurate results due to the guidance of landmarks. In each process of registration, with the estimated motion between atlas and target images, each atlas label is also warped to provide an estimate for the target label using the same motion field. All the warped estimates of target labels are fused by deep fusion net to generate a final prediction of target label.

3.3. Parameter settings

Empirically, we fix the learning rate of deep fusion net to 5×10^{-7} and the size of search window in the shift layer to 7×7, which will be utilized in all of the following experiments except the evaluations of different search volumes. Besides, we utilize 4 convolutional layers with strides of 1, and these layers

[3] http://www.itk.org/

respectively have 64 filters in size of $5 \times 5 \times 1$, 64 filters in size of $5 \times 5 \times 64$, 128 filters in size of $5 \times 5 \times 64$, and 128 filters in size of $5 \times 5 \times 128$. In the current study, our proposed method processes cardiac MR images slice by slice. As for the image size, the average size of ROIs in SATA-13 database is about 110×140, while the ROIs in LV-09 database are around 135×155.

3.4. Segmentation accuracy

The quantitative segmentation results are reported on SATA-13 database in Table 1 and LV-09 database in Tables 2-5. For fair comparison, all the registration-based methods use the LB registration framework introduced in section 3.2, except for methods marked by (LF) using the landmark-free registration.

3.4.1. SATA-13 database

For SATA-13 database, we compare the segmentation accuracy of deep fusion net with the ones of majority voting (MV), patch-based segmentation (PB) (Coupé et al., 2011), as well as SVM-based segmentation with augmented features (SVMAF) (Bai et al., 2015). Besides, another version of deep fusion net which uses normalized mutual information (NMI) as similarity measure for atlas selection at testing process, denoted as DFN_NMI, is also included in the comparison. The results of MV, PB and SVMAF are reproduced by the published codes [4] using the same parameter settings in Bai et al. (2015) based on the LB registration. The segmentation accuracy is evaluated by averaged Dice metric (ADM, higher value means better performance) and averaged Hausdorff distance (AHD, lower value means better performance) of the myocardium across ED frame and all the testing subjects in 5-fold cross validation.

As shown in Table 1, both DFN and DFN_NMI achieve better segmentation accuracies than the methods of MV, PB and SVMAF in both two metrics when using LB registration. Besides, our DFN based on LF registration, *i.e.*, DFN(LF), also obtains higher accuracy in ADM than these compared methods based on LB registration, indicating that deep fusion net performs well in segmenting LV even for insufficient registration quality without using landmarks. Compared with NMI, our defined deep feature distance works especially well for atlas selection in case of LF registration (please refer to DFN(LF) and DFN_NMI(LF) in Table 1), improving ADM from 0.802 to 0.815 and AHD from 27.00 to 18.33. As for LB registration, this improvement is marginal, possibly because the registration quality is high when using LB registration with the help of landmarks.

Convolutional neural network (CNN) is also included in this comparison to evaluate the effect of NL-PLF subnet, and we restrict that the CNN and our DFN have the identical network capacity of feature extraction, *i.e.*, the compared CNN in Table 1 has the same feature extraction subnet as ours in section 3.3, which is then followed by a convolutional layer and a softmax layer

[4] `http://wp.doc.ic.ac.uk/wbai/software/`

Method	Averaged Dice Metric (ADM)	Averaged Hausdorff Distance (AHD)
DFN	**0.833**(**0.039**)	**11.35**(**3.53**)
DFN(LF)	0.815(0.044)	18.33(8.98)
DFN_NMI	0.831(0.039)	11.98(3.84)
DFN_NMI(LF)	0.802(0.051)	27.00(12.75)
SVMAF	0.777(0.057)	17.31(4.40)
PB	0.761(0.056)	12.11(3.86)
MV	0.747(0.057)	12.16(3.87)
CNN	0.695(0.092)	52.33(11.59)
DFN(crossDB)	0.815(0.040)	11.76(3.70)
DFN_NMI(crossDB)	0.809(0.040)	12.46(4.19)

Table 1: Segmentation accuracies of different methods on SATA-13 database. Each cell is formatted as "mean (standard deviation)".

to output the target label. Experimental results show that our DFN achieves significantly higher accuracies than CNN in all metrics, indicating the effectiveness of NL-PLF subnet.

Figure 4 compares the segmentation accuracies in a box-plot, showing that our DFN and DFN_NMI achieve much higher median values and more robust results than other multi-atlas segmentation methods when using LB registration. Figure 5 shows visual examples of the segmentation results by different methods on the basal, mid-ventricular and apical slices from a testing subject.

3.4.2. LV-09 database

For LV-09 database, we compare the epicardium and endocardium segmentation accuracies of the testing and online sets in Tables 2, 4 and Tables 3, 5. Similar to Ngo et al. (2017), both ED and ES frames are evaluated to measure accuracies for endocardium segmentation, while only ED frame is evaluated for the epicardium segmentation. Besides the traditional multi-atlas segmentation methods, we also compare two recent deep learning-based methods that achieve state-of-the-art results on this database, *i.e.* the combined stacked autoencoder and level set method (SAELS) (Avendi et al., 2016) and the combined deep belief network and level set method (DBNLS) (Ngo et al., 2017). Both SAELS and DBNLS first utilize deep network to estimate an initial segmentation result, which is then refined by level set approach to produce a final estimation. More exactly, DBNLS respectively trains four DBNs for epicardium or endocardium at ED or ES frame, and SAELS respectively trains two networks for large-contour or small-contour images on endocardium segmentation. Similarly, we respectively learn three different deep fusion nets for epicardium at ED, endocardium at ED and endocardium at ES. Besides, DBNLS utilizes the training and on-

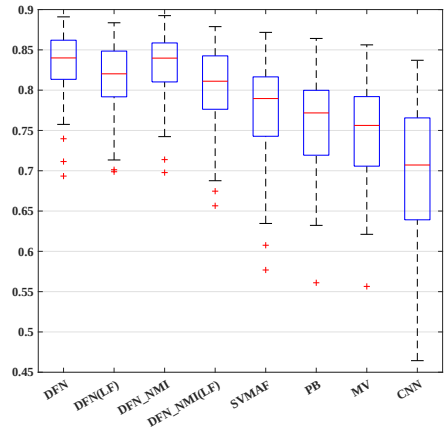

Fig. 4: Comparison of the segmentation accuracies for different methods on SATA-13 database in terms of Dice metric. The red central mark of the box is the median and the edges are the 25th and 75th percentiles, while the red plus signs represent outliers.

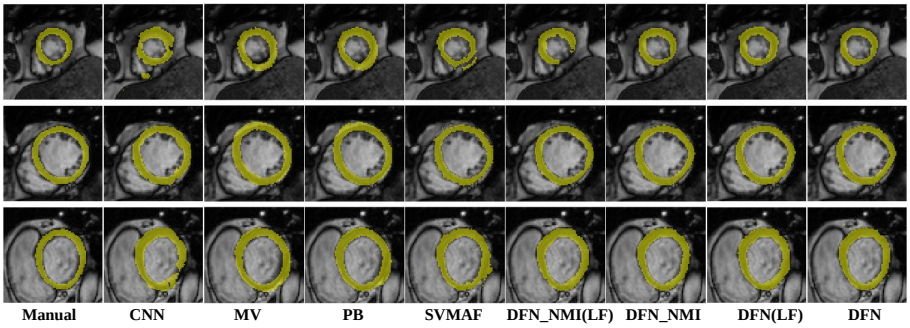

Fig. 5: Visual comparison of segmentation results using different methods on SATA-13 database. Please refer to the electronic version for better comparison. Top to bottom: the basal, mid-ventricular and apical slices from the same testing subject. Left to right: manual labeling, convolutional neural network (CNN), majority voting (MV), patch-based method (PB), SVM segmentation with augmented features (SVMAF), DFN_NMI using LF registration, DFN_NMI, DFN using LF registration, and DFN.

line sets for model training, and reports the performance on testing set, while SAELS has the same experimental setting with us, *i.e.*, training on training set and reporting results on testing and online sets.

Method	"Good" percentage	Epicardium ADM	Epicardium APD
DFN	**100**(**0**)	0.95(0.01)	1.90(0.22)
DFN(LF)	78.90(20.58)	0.94(0.01)	2.55(0.80)
DFN_NMI	98.67(3.52)	**0.96**(**0.01**)	1.88(0.18)
DFN_NMI(LF)	66.15(21.00)	0.93(0.03)	2.80(0.86)
DBNLS(semi)	**100**(**0**)	0.94(0.01)	**1.73**(**0.28**)
DBNLS	94.65(6.18)	0.93(0.02)	2.08(0.60)
SVMAF	95.43(8.03)	0.93(0.01)	2.85(0.50)
PB	94.60(8.17)	0.93(0.02)	2.54(0.41)
MV	94.60(8.17)	0.93(0.02)	2.57(0.41)

Table 2: **Epicardium** segmentation accuracies of different methods on **testing set** of LV-09 database, where only training set is used as training data. Each cell is formatted as "mean (standard deviation)".

Method	"Good" percentage	Endocardium ADM	Endocardium APD
DFN	97.58(7.12)	0.92(0.04)	2.04(0.44)
DFN(LF)	73.56(29.00)	0.91(0.06)	2.31(0.40)
DFN_NMI	97.25(7.24)	0.92(0.04)	2.05(0.42)
DFN_NMI(LF)	66.61(29.59)	0.92(0.03)	2.35(0.47)
DBNLS(semi)	**100**(**0**)	0.91(0.03)	1.79(0.36)
DBNLS	95.91(5.28)	0.88(0.03)	2.34(0.46)
SAELS	97.8(4.7)	**0.94**(**0.02**)	**1.7**(**0.37**)
SAELS(init)	90(10)	0.90(0.1)	2.84(0.29)
SVMAF	94.79(11.06)	0.88(0.04)	3.00(0.51)
PB	92.11(12.00)	0.87(0.06)	2.76(0.54)
MV	91.08(15.11)	0.87(0.05)	2.77(0.53)

Table 3: **Endocardium** segmentation accuracies of different methods on **testing set** of LV-09 database, where only training set is used as training data. Each cell is formatted as "mean (standard deviation)".

As shown in Tables 2 and 4, for the epicardium segmentation, our proposed methods (referred as DFN and DFN_NMI) achieve higher accuracies than other methods in all metrics except DBNLS(semi) using manually-labeled segmentation masks as prior, which will be further discussed in the next paragraph. For

Method	"Good" percentage	Epicardium ADM	Epicardium APD
DFN	93.62(13.55)	**0.95**(**0.01**)	1.98(0.27)
DFN(LF)	65.40(29.46)	0.93(0.04)	2.73(0.68)
DFN_NMI	92.53(13.58)	**0.95**(**0.01**)	2.01(0.32)
DFN_NMI(LF)	50.54(27.29)	0.93(0.03)	2.91(0.79)
DBNLS(semi)	**100**(**0**)	0.94(0.02)	**1.90**(**0.53**)
DBNLS	84.32(23.45)	0.93(0.03)	2.05(0.61)
SVMAF	84.84(21.74)	0.93(0.01)	3.01(0.47)
PB	92.34(13.16)	0.92(0.02)	2.77(0.43)
MV	92.34(13.16)	0.92(0.02)	2.80(0.42)

Table 4: **Epicardium** segmentation accuracies of different methods on **online set** of LV-09 database, where only training set is used as training data. Each cell is formatted as "mean (standard deviation)".

Method	"Good" percentage	Endocardium ADM	Endocardium APD
DFN	96.36(8.41)	0.92(0.03)	2.06(0.58)
DFN(LF)	60.87(26.48)	**0.93**(**0.02**)	2.41(0.47)
DFN_NMI	95.41(9.43)	0.92(0.04)	2.04(0.53)
DFN_NMI(LF)	53.81(25.88)	0.90(0.07)	2.66(0.65)
DBNLS(semi)	**100**(**0**)	0.91(0.03)	**1.78**(**0.49**)
DBNLS	90.54(14.40)	0.89(0.03)	2.17(0.46)
SAELS	95.58(6.7)	**0.93**(**0.02**)	1.92(0.51)
SAELS(init)	87(12)	0.89(0.03)	2.95(0.54)
SVMAF	92.86(12.65)	0.89(0.05)	2.82(0.60)
PB	91.71(14.20)	0.88(0.05)	2.65(0.55)
MV	90.32(14.64)	0.88(0.05)	2.73(0.56)

Table 5: **Endocardium** segmentation accuracies of different methods on **online set** of LV-09 database, where only training set is used as training data. Each cell is formatted as "mean (standard deviation)".

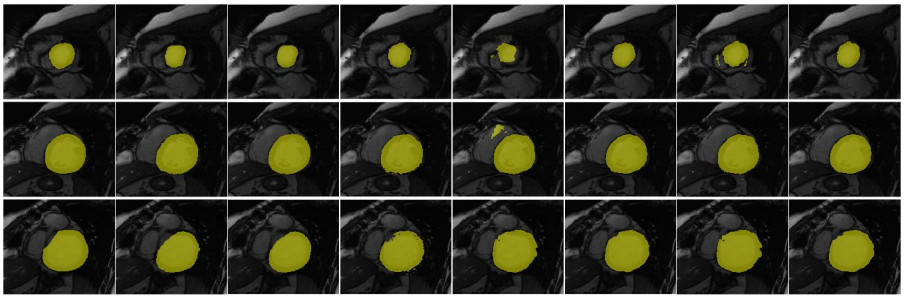

(a) Epicardium segmentation results at ED frame.

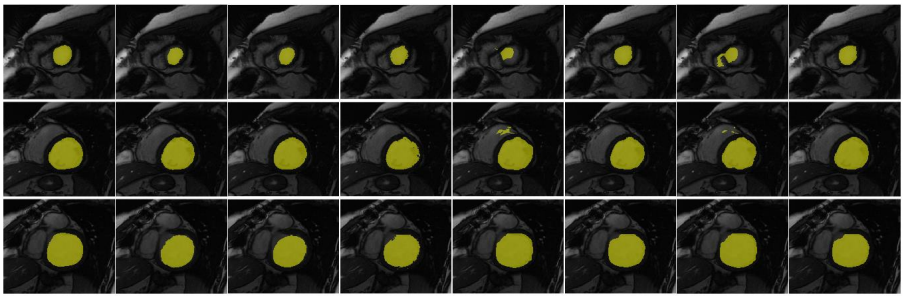

(b) Endocardium segmentation results at ED frame.

Fig. 6: Segmentation results using different methods on LV-09 database. Epicardium slices in (a) and Endocardium slices in (b) are from one subject in the testing set. Top to bottom: the basal, mid-ventricular and apical slices from the same subject. Left to right: manual labeling, majority voting (MV), patch-based method (PB), SVM segmentation with augmented features (SVMAF), DFN_NMI using LF registration, DFN_NMI, DFN using LF registration, and DFN.

the endocardium segmentation, our methods get the highest ADM except for SAELS, which utilizes level set method to refine the initial segmentation by stacked autoencoder. Without the deformable model, SAELS reports the endocardium segmentation accuracies of 0.90 in testing set and 0.89 in online set, compared with 0.92 and 0.92 of ours purely based on thresholding the estimated label probability map of deep networks, as shown in Tables 3 and 5.

As shown in Tables 2-5, our method of DFN generally outperforms DBNLS (except DBNLS(semi)) in all metrics on testing and online sets, while the standard deviations are almost on the same level. DBNLS(semi) is a semi-automated method using DBN for segmentation, but relying on manually-labeled segmentation masks as prior, and the segmentation results are also refined by level set method. It achieves high accuracy largely due to the manually-labeled segmentation masks, while our DFN does not depend on extra labeled segmentation prior. Compared with this semi-automated method, our proposed DFN achieves better ADM scores but comparable "Good" percentage and APD.

Due to the inaccurate registration without using landmarks, our proposed DFN(LF) achieves relatively lower values of "Good" percentage and comparable values of ADM and APD in all comparisons. Figure 6 shows the segmentation results of different methods. These results are for epicardium and endocardium segmentations of the basal, mid-ventricular and apical slices from one subject in the testing set.

3.5. Impact of atlas selection strategy

In the training and testing phases of our DFNs, we could choose different atlas selection strategies, *e.g.*, selecting different numbers of atlases, using either deep feature distance or NMI for atlas selection. In this section, we will test the impacts of different atlas selection strategies on the performance of DFN.

We first compare the segmentation accuracies of our proposed methods (referred to DFN_NMI and DFN) with respect to different numbers of selected atlases at testing phase. The deep fusion nets learned in sections 3.4.1 and 3.4.2, which use randomly selected 5 atlases based on NMI at training phase, are utilized in this comparison. As shown in Fig. 7, we compare the performance of DFN_NMI and DFN on SATA-13 database (Fig. 7a and 7b) and LV-09 database (Fig. 7c and 7d) respectively. As we can see, atlas selection using deep feature distance consistently works better than that using NMI for different numbers of selected atlases at testing phase. Moreover, using larger number of atlases generally produce better ADM scores, but the accuracies saturate after around 11 atlases.

We next justify the advantages of our random atlas selection strategy at training phase, as discussed in section 2.4. By fixing the number of selected atlases to 5, we compare the performance of DFNs using three different atlas selection strategies in each forward-backward computation of training process, *i.e.*, selecting top-5 atlases with smallest deep feature distances (top5_DF), selecting top-5 atlases with largest normalize mutual information (top5_NMI), and randomly selecting atlases according to a distribution proportional to NMI between target image and atlases (random5_NMI). We train DFNs with the

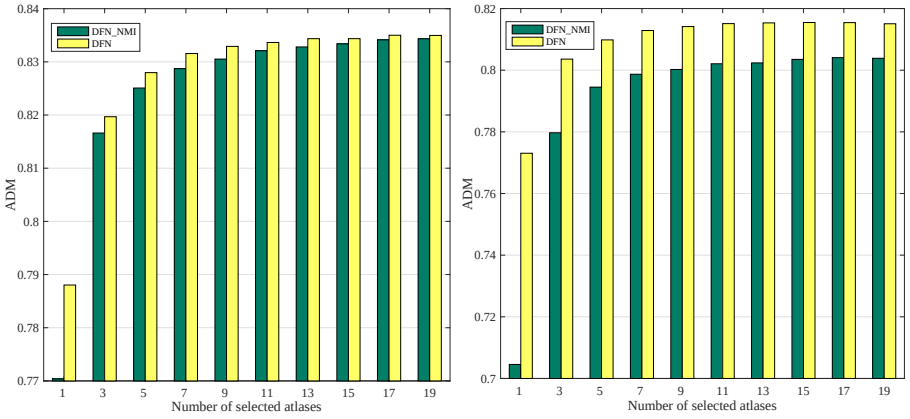

(a) SATA-13 (LB Registration)

(b) SATA-13 (LF Registration)

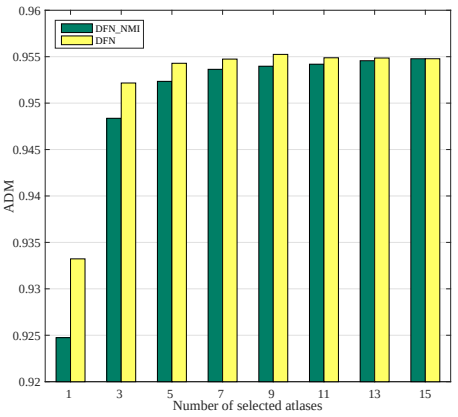

(c) LV-09 (Epicardium)

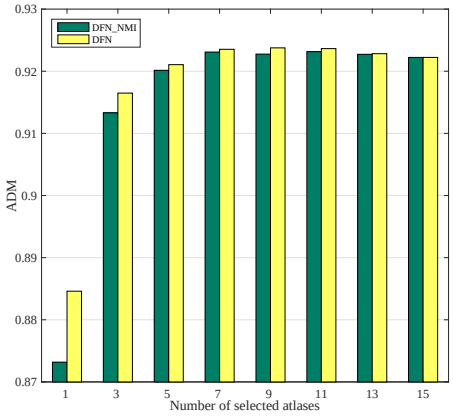

(d) LV-09 (Endocardium)

Fig. 7: The change of averaged 3D Dice metric *w.r.t.* the number of selected atlases in the testing process. (a) and (b) are respectively for LB registration and LF registration on SATA-13 database, while (c) and (d) are for epicardium and endocardium utilizing LB registration on LV-09 database.

above strategies for epicardium at ED using 15 training subjects, and test on 30 testing and online subjects of LV-09 database. For each strategy at training phase, we attempt two different atlas selection strategies at testing phase, *i.e.*, select top-5 atlases with largest normalize mutual information (top5_NMI) and select top-5 atlases with smallest deep feature distance (top5_DF). The experimental results are listed in Table 6. Compared with the strategies of top5_DF and top5_NMI at training phase, the strategy of using random5_NMI performs best in all metrics. Moreover, random5_NMI paired with top5_DF strategies at training and testing phases achieves the best accuracies among all the compared strategies.

Training	Testing	"Good" percentage	ADM	APD
Random5_NMI	Top5_DF	**97.59**(**6.18**)	0.9499(0.01)	**1.97**(**0.30**)
	Top5_NMI	95.71(9.34)	**0.9503**(**0.01**)	2.01(0.30)
Top5_DF	Top5_DF	97.40(6.46)	0.9483(0.01)	2.00(0.33)
	Top5_NMI	94.59(10.26)	0.9488(0.01)	2.03(0.29)
Top5_NMI	Top5_DF	96.90(8.99)	0.9468(0.01)	2.02(0.32)
	Top5_NMI	95.30(10.51)	0.9472(0.01)	2.05(0.33)

Table 6: Segmentation accuracies of DFNs with different atlas selection strategies at training and testing phases on **testing and online sets** of LV-09 database, where only training set is used as training data. Each cell is formatted as "mean (standard deviation)".

In Table 7, we also compare the performance of DFN by varying the numbers of selected atlases (denoted as K_0) at training phase using random atlas selection strategy, with K_0 atlases selected by deep feature distance at testing phase. The experimental results show that the segmentation accuracies are relatively stable to K_0, *e.g.*, the accuracies are not significantly lower even when using 1 training atlas (*i.e.*, $K_0 = 1$), this is probably because the random atlas selection strategy enforces that each target image at training phase can be paired with diverse atlases. Empirically, K_0 with values of 5 to 7 produces best accuracies.

3.6. Impact of search volume

We now evaluate the influence of search volume R_{nl}, *i.e.*, the non-local region for patch-based label fusion, on the segmentation performance. As shown in Table 8, we respectively train five DFNs with different search volumes, whose sizes range from 1 to 9 with interval of 2, on epicardium at ED frame using 15 training subjects, and test on 30 testing and online subjects of LV-09 database. The random atlas selection strategy and deep feature distance are respectively utilized at training and testing phases, while the number of selected atlases is fixed as 5 for both phases. The results indicate that the segmentation accuracies are not sensitive to search volume, and generally a larger size of search volume could produce marginally better segmentation accuracies. This is reasonable

K_0	"Good" percentage	ADM	APD
1	95.66(9.60)	0.9335(0.02)	2.34(0.50)
3	97.17(6.43)	0.9463(0.01)	2.07(0.37)
5	**97.59**(**6.18**)	**0.9499**(**0.01**)	1.97(0.30)
7	97.14(8.78)	**0.9499**(**0.01**)	**1.93**(**0.29**)
9	96.25(10.00)	0.9496(0.01)	1.97(0.29)

Table 7: Segmentation accuracies by training DFNs with different numbers of selected atlases K_0 on training set and testing on **testing and online sets** of LV-09 database. The size of search volume is fixed as [7,7], and the number of selected atlases for testing is same as the corresponding training one. Each cell is formatted as "mean (standard deviation)".

since larger search volume provides more patch candidates around registered pixels for label fusion, resulting in robustness to inaccurate registrations.

R_{nl}	"Good" percentage	ADM	APD
$[1, 1]$	97.35(6.50)	0.9418(0.01)	2.17(0.36)
$[3, 3]$	96.15(11.72)	0.9453(0.01)	2.10(0.35)
$[5, 5]$	96.03(9.47)	0.9483(0.01)	1.96(0.30)
$[7, 7]$	97.59(6.18)	0.9499(0.01)	1.97(0.30)
$[9, 9]$	**97.89**(**6.06**)	**0.9507**(**0.01**)	**1.94**(**0.32**)

Table 8: Segmentation accuracies by training DFNs with different sizes of search volumes R_{nl} on training set and testing on **testing and online sets** of LV-09 database. The number of selected atlases is fixed as 5 for training and testing. Each cell is formatted as "mean (standard deviation)".

3.7. Cross-database evaluation

To evaluate the generalization abilities of the learned DFNs across different databases, we conduct experimental comparisons for network training and testing across two different databases. More specifically, we train each DFN on one database and test it on the other one. When we test the DFN learned from training database on the testing database, we attempt two different atlas selection strategies for the testing subjects, *i.e.*, selecting atlases from the subjects in the training database or in the testing database. Since the SATA-13 database provides the segment masks and LV-09 database only provides contour labels, we transfer the contour labels of LV-09 database to segment masks as segmentation labels, in order to keep the labels of two databases consistent. The experiments are performed on ED frame of both databases, and the accuracy is evaluated by averaged Dice metric and averaged Hausdorff distance over all subjects at ED frame of the testing database.

We first evaluate the cross-database performance using the strategy that selects atlases from the subjects in the training database for the testing subjects in the testing database, and the segmentation accuracies are listed in Tables 9 (train DFN on LV-09 and test it on SATA-13) and 10 (train DFN on SATA-13 and test it on LV-09). The experimental results show that our learned DFNs achieve significantly higher ADMs and slightly better AHDs than traditional multi-atlas segmentation methods on both two databases. Compared with the methods that perform training and testing on the same database, *e.g.*, Table 1 in section 3.4.1, the accuracies of our DFN for cross-database evaluation are relatively low, which is possibly because of the different styles of manual labels in these two databases, as shown in Fig. 8 (please refer to the figure for detailed descriptions of this difference). Figure 9 shows the performance of our proposed methods with different numbers of selected atlases respectively on two databases in the testing process, indicating that our defined deep feature distance consistently works better than NMI in all metrics, while a small number of selected atlases would enlarge this advantage.

We also evaluate the cross-database performance using the strategy that selects atlases from the subjects in the testing database for the testing subjects also in the testing database. In Table 1, we present the results of our methods (denoted as DFN(crossDB) and DFN_NMI(crossDB)) by applying the DFN learned from LV-09 database to the SATA-13 database without fine-tuning. These accuracies are calculated using the same 5-fold cross validation utilized in section 3.4.1. The experimental results show that, if the subjects in SATA-13 database are used as atlases for testing, the DFN learned from LV-09 database can achieve comparable results on SATA-13 database in all metrics, compared with those segmentation methods training and testing on the same SATA-13 database. This justifies that our learned feature extraction subnet has well generalization ability across different databases for the LV segmentation task.

Method	Averaged Dice Metric	Averaged Hausdorff Distance
DFN	**0.734**(**0.058**)	**15.32**(**3.88**)
DFN_NMI	0.730(0.060)	15.82(4.44)
SVMAF	0.691(0.082)	22.15(5.82)
PB	0.639(0.067)	16.69(3.26)
MV	0.620(0.066)	16.58(3.22)

Table 9: Segmentation results by training DFNs on LV-09 database and testing on SATA-13 database, where 45 subjects of LV-09 database are used as atlases in the testing process. Each cell is formatted as "mean (standard deviation)".

3.8. Results on SATA-13 testing dataset

All the previous experiments about SATA-13 database are performed on Cardiac Atlas Project (CAP) training set of MICCAI 2013 SATA Segmentation

Method	Averaged Dice Metric	Averaged Hausdorff Distance
DFN	**0.766**(**0.042**)	**10.68**(**3.84**)
DFN_NMI	0.763(0.044)	11.95(4.78)
SVMAF	0.708(0.044)	17.63(4.93)
PB	0.681(0.055)	11.45(2.55)
MV	0.672(0.057)	11.83(3.10)

Table 10: Segmentation results by training DFNs on SATA-13 database and testing on LV-09 database, where 83 subjects of SATA-13 database are used as atlases in the testing process. Each cell is formatted as "mean (standard deviation)".

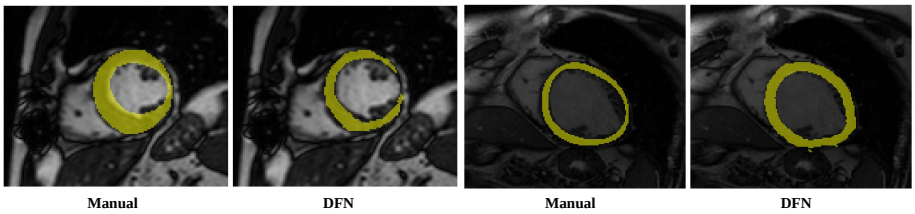

(a) Testing on SATA-13 database (b) Testing on LV-09 database

Fig. 8: Visual examples of estimated segmentations by DFN (right) and corresponding manual segmentations (left) in (a) SATA-13 database and (b) LV-09 database. As we can see, manual segmentation in (a) SATA-13 database is much "thicker" than the one in (b) LV-09 database. In (b) LV-09 database, the estimated segmentation by DFN is much "thicker" than the manual one, possibly because the network here is trained on "thick" labels of SATA-13 database and utilizes "thick" atlases to estimate the target label. Similarly, the estimated segmentation in (a) SATA-13 database is much "thinner" than the manual one.

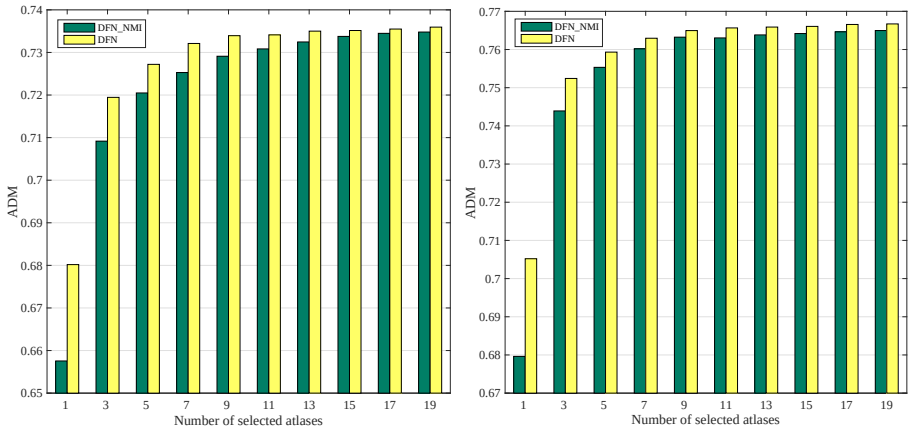

(a) Testing accuracy on SATA-13 database (b) Testing accuracy on LV-09 database

Fig. 9: The change of averaged Dice metric *w.r.t.* the number of selected atlases respectively on (a) SATA-13 database and (b) LV-09 database in the testing process.

Challenge, which contains 83 subjects with the ground-truth segmentations. To compare with other state-of-the-art methods, we train a deep fusion net on CAP training set and test its performance on CAP testing set of the challenge, whose ground-truth segmentations are unknown to challenge participants. We submit our segmentation results to the challenge website, and the corresponding testing accuracies are evaluated by the website and published on its leaderboard [5,6].

As shown on the leaderboard, our proposed methods based on LB and LF registrations (referred as DeepMAS_LB and DeepMAS_LF) respectively achieve 0.815 and 0.799 in Dice metric. Until Sep. 2017, our method based on LB registration ranked first in Dice metric on the leaderboard of "Cardiac Atlas Project (CAP) - Free Competition" in MICCAI 2013 SATA Segmentation Challenge.

4. Discussions

Comparisons with related deep neural networks. Our proposed method learns an embedding space by feature extraction subnet at training phase, which is then utilized to define a deep feature distance for atlas selection at testing phase. Similarly, some works in computer vision also define image similarities based on the learned embedding spaces by deep convolutional networks. For example, Schroff et al. (2015) presented a network that directly learned a mapping from face images to a compact Euclidean space where the distance directly corresponded to a measure of face similarity. Zheng et al. (2016) proposed a siamese network with two losses to learn a discriminative CNN embedding and a similarity metric simultaneously. However, compared with these methods learning image similarities directly enforced by network losses, our proposed method computes the similarities between target and atlas images for estimating label fusion weights, which is to minimize the loss between the estimated and ground-truth target segmentations.

Computational consumptions and network extensions. Currently, our implementation is based on the MatConvNet library [7], and all experiments are performed on a Dell Precision T7910 workstation with GeForce GTX TITAN X (12GB) on a Ubuntu platform. For a target image in size of 120×140 with $K_0 = 5$, a deep fusion net, which uses the parameter settings in section 3.3, respectively needs about 0.30 second and 0.31 second for one forward and backward processes. In this case, the maximum allowed number of selected atlases K_0 for training is up to 42. Although our proposed framework can be scaled up to 3D theoretically, the present study is based on 2D images mainly due to the constraint of GPU memory, which is also the biggest challenge for the other deep learning approaches. Currently, one common solution for this problem is to train the networks using 3D patches instead of full 3D images (Kamnitsas

[5] Old website: http://masi.vuse.vanderbilt.edu/submission/leaderboard.html

[6] New website: https://www.synapse.org/#!Synapse:syn3193805/wiki/217788 (Last accessed: 15 Sep 2017)

[7] http://www.vlfeat.org/matconvnet/

et al., 2017; Rajchl et al., 2017; Dou et al., 2017), which would be one of our future directions.

5. Conclusions

In this work, we accomplish the multi-atlas segmentation framework by a specially designed convolutional neural network, aiming to extract the optimal deep features for a specific segmentation task by an end-to-end training strategy. Besides, the extracted deep features are further utilized to define a similarity measure for atlas selection at testing phase. The proposed method is evaluated on two publicly available databases of SATA-13 and LV-09 for left ventricle segmentation, and experimental results demonstrate that our approach achieves the state-of-the-art accuracies on both databases. In future, we plan to apply this idea to other atlas-based segmentation tasks, *e.g.*, brain, abdominal organs, *etc.* Besides, we are also interested in applying the proposed framework to 3D images for further improving the segmentation accuracy.

Acknowledgments

This work was supported by the National Natural Science Foundation of China (NSFC) under Grant No. 61472313, 11622106, 11401464 and 91330204, International Exchange Foundation of China NSFC and United Kingdom RS under grant No. 61711530242 and the National Basic Research Program of China under Grant No. 2013CB329404.

References

References

Aljabar, P., Heckemann, R., Hammers, A., Hajnal, J., Rueckert, D., 2009. Multi-atlas based segmentation of brain images: Atlas selection and its effect on accuracy. NeuroImage 46, 726 – 738. doi:10.1016/j.neuroimage.2009.02.018.

Artaechevarria, X., Munoz-Barrutia, A., de Solorzano, C.O., 2009. Combination strategies in multi-atlas image segmentation: Application to brain MR data. IEEE Transactions on Medical Imaging 28, 1266–1277. doi:10.1109/TMI.2009.2014372.

Asman, A.J., Huo, Y., Plassard, A.J., Landman, B.A., 2015. Multi-atlas learner fusion: An efficient segmentation approach for large-scale data. Medical Image Analysis 26, 82 – 91. doi:10.1016/j.media.2015.08.010.

Asman, A.J., Landman, B.A., 2013. Non-local statistical label fusion for multi-atlas segmentation. Medical Image Analysis 17, 194 – 208. doi:10.1016/j.media.2012.10.002.

Avendi, M., Kheradvar, A., Jafarkhani, H., 2016. A combined deep-learning and deformable-model approach to fully automatic segmentation of the left ventricle in cardiac MRI. Medical Image Analysis 30, 108 – 119. doi:10.1016/j.media.2016.01.005.

Bai, W., Shi, W., Ledig, C., Rueckert, D., 2015. Multi-atlas segmentation with augmented features for cardiac MR images. Medical image analysis 19, 98–109. doi:10.1016/j.media.2014.09.005.

Bai, W., Shi, W., O'Regan, D.P., Tong, T., Wang, H., Jamil-Copley, S., Peters, N.S., Rueckert, D., 2013. A probabilistic patch-based label fusion model for multi-atlas segmentation with registration refinement: Application to cardiac MR images. IEEE Transactions on Medical Imaging 32, 1302–1315. doi:10.1109/TMI.2013.2256922.

Cardoso, M.J., Leung, K., Modat, M., Keihaninejad, S., Cash, D., Barnes, J., Fox, N.C., Ourselin, S., 2013. STEPS: Similarity and truth estimation for propagated segmentations and its application to hippocampal segmentation and brain parcelation. Medical Image Analysis 17, 671 – 684. doi:10.1016/j.media.2013.02.006.

Chen, H., Qi, X., Yu, L., Dou, Q., Qin, J., Heng, P.A., 2017. DCAN: Deep contour-aware networks for object instance segmentation from histology images. Medical Image Analysis 36, 135 – 146. doi:10.1016/j.media.2016.11.004.

Collignon, A., Maes, F., Delaere, D., Vandermeulen, D., Suetens, P., Marchal, G., 1995. Automated multi-modality image registration based on information theory, in: Bizais, Y., Barillot, C., Paola, R. (Eds.), Information Processing in Medical Imaging (IPMI) 1995, Kluwer Academic Publishers, Dordrecht. pp. 263–274.

Commowick, O., Warfield, S.K., Malandain, G., 2009. Using Frankenstein's creature paradigm to build a patient specific atlas, in: Medical Image Computing and Computer-Assisted Intervention (MICCAI) 2009, Springer Berlin Heidelberg. pp. 993–1000. doi:10.1007/978-3-642-04271-3_120.

Coupé, P., Manjón, J.V., Fonov, V., Pruessner, J., Robles, M., Collins, D.L., 2011. Patch-based segmentation using expert priors: Application to hippocampus and ventricle segmentation. NeuroImage 54, 940 – 954. doi:10.1016/j.neuroimage.2010.09.018.

Dou, Q., Yu, L., Chen, H., Jin, Y., Yang, X., Qin, J., Heng, P.A., 2017. 3D deeply supervised network for automated segmentation of volumetric medical images. Medical Image Analysis 41, 40–54. doi:10.1016/j.media.2017.05.001.

Duc, A.K.H., Modat, M., Leung, K.K., Cardoso, M.J., Barnes, J., Kadir, T., Ourselin, S., Initiative, A.D.N., 2013. Using manifold learning for atlas selection in multi-atlas segmentation. PLoS ONE 8, 1–11. doi:10.1371/journal.pone.0070059.

Fu, H., Xu, Y., Lin, S., Kee Wong, D.W., Liu, J., 2016. DeepVessel: Retinal vessel segmentation via deep learning and conditional random field, in: Medical Image Computing and Computer-Assisted Intervention (MICCAI) 2016, Springer International Publishing. pp. 132–139. doi:10.1007/978-3-319-46723-8_16.

Goodfellow, I., Bengio, Y., Courville, A., 2016. Deep Learning. MIT Press. URL: www.deeplearningbook.org.

Guo, Y., Gao, Y., Shen, D., 2016. Deformable MR prostate segmentation via deep feature learning and sparse patch matching. IEEE Transactions on Medical Imaging 35, 1077–1089. doi:10.1109/TMI.2015.2508280.

Havaei, M., Davy, A., Warde-Farley, D., Biard, A., Courville, A., Bengio, Y., Pal, C., Jodoin, P.M., Larochelle, H., 2017. Brain tumor segmentation with deep neural networks. Medical Image Analysis 35, 18 – 31. doi:10.1016/j.media.2016.05.004.

Heckemann, R.A., Hammers, A., Aljabar, P., Rueckert, D., Hajnal, J.V., 2009. The mirror method of assessing segmentation quality in atlas label propagation, in: International Symposium on Biomedical Imaging (ISBI) 2009, pp. 1194–1197. doi:10.1109/ISBI.2009.5193272.

Hinton, G., Salakhutdinov, R., 2006. Reducing the dimensionality of data with neural networks. Science 313, 504507. doi:10.1126/science.1127647.

Iglesias, J.E., Sabuncu, M.R., 2015. Multi-atlas segmentation of biomedical images: a survey. Medical image analysis 24, 205–219.

Isgum, I., Staring, M., Rutten, A., Prokop, M., Viergever, M.A., van Ginneken, B., 2009. Multi-atlas-based segmentation with local decision fusion: Application to cardiac and aortic segmentation in CT scans. IEEE Transactions on Medical Imaging 28, 1000–1010. doi:10.1109/TMI.2008.2011480.

Kamnitsas, K., Ledig, C., Newcombe, V.F., Simpson, J.P., Kane, A.D., Menon, D.K., Rueckert, D., Glocker, B., 2017. Efficient multi-scale 3D CNN with fully connected CRF for accurate brain lesion segmentation. Medical Image Analysis 36, 61 – 78. doi:10.1016/j.media.2016.10.004.

Khalaf, A.F., Yassine, I.A., Fahmy, A.S., 2016. Convolutional neural networks for deep feature learning in retinal vessel segmentation, in: International Conference on Image Processing (ICIP) 2016, pp. 385–388. doi:10.1109/ICIP.2016.7532384.

Krizhevsky, A., Sutskever, I., Hinton, G.E., 2012. Imagenet classification with deep convolutional neural networks, in: Advances in neural information processing systems, pp. 1097–1105.

Makropoulos, A., Gousias, I.S., Ledig, C., Aljabar, P., Serag, A., Hajnal, J.V., Edwards, A.D., Counsell, S.J., Rueckert, D., 2014. Automatic whole brain MRI segmentation of the developing neonatal brain. IEEE Transactions on Medical Imaging 33, 1818–1831. doi:10.1109/TMI.2014.2322280.

Maninis, K.K., Pont-Tuset, J., Arbeláez, P., Van Gool, L., 2016. Deep retinal image understanding, in: Medical Image Computing and Computer-Assisted Intervention (MICCAI) 2016, Springer International Publishing. pp. 140–148. doi:10.1007/978-3-319-46723-8_17.

Moeskops, P., Viergever, M.A., Mendrik, A.M., de Vries, L.S., Benders, M.J.N.L., Igum, I., 2016. Automatic segmentation of MR brain images with a convolutional neural network. IEEE Transactions on Medical Imaging 35, 1252–1261. doi:10.1109/TMI.2016.2548501.

Ngo, T.A., Lu, Z., Carneiro, G., 2017. Combining deep learning and level set for the automated segmentation of the left ventricle of the heart from cardiac cine magnetic resonance. Medical Image Analysis 35, 159 – 171. doi:10.1016/j.media.2016.05.009.

Petitjean, C., Dacher, J.N., 2011. A review of segmentation methods in short axis cardiac MR images. Medical Image Analysis 15, 169 – 184. doi:10.1016/j.media.2010.12.004.

Pouch, A., Wang, H., Takabe, M., Jackson, B., III, J.G., Gorman, R., Yushkevich, P., Sehgal, C., 2014. Fully automatic segmentation of the mitral leaflets in 3D transesophageal echocardiographic images using multi-atlas joint label fusion and deformable medial modeling. Medical Image Analysis 18, 118 – 129. doi:10.1016/j.media.2013.10.001.

Radau, P., Lu, Y., Connelly, K., Paul, G., Dick, A., Wright, G., 2009. Evaluation framework for algorithms segmenting short axis cardiac MRI. Midas Journal URL: http://hdl.handle.net/10380/3070.

Rajchl, M., Lee, M.C.H., Oktay, O., Kamnitsas, K., Passerat-Palmbach, J., Bai, W., Damodaram, M., Rutherford, M.A., Hajnal, J.V., Kainz, B., Rueckert, D., 2017. DeepCut: Object segmentation from bounding box annotations using convolutional neural networks. IEEE Transactions on Medical Imaging 36, 674–683. doi:10.1109/TMI.2016.2621185.

Sanroma, G., Wu, G., Gao, Y., Shen, D., 2014. Learning to rank atlases for multiple-atlas segmentation. IEEE Transactions on Medical Imaging 33, 1939–1953. doi:10.1109/TMI.2014.2327516.

Sanroma, G., Wu, G., Gao, Y., Thung, K.H., Guo, Y., Shen, D., 2015. A transversal approach for patch-based label fusion via matrix completion. Medical Image Analysis 24, 135 – 148. doi:10.1016/j.media.2015.06.002.

Schroff, F., Kalenichenko, D., Philbin, J., 2015. FaceNet: A unified embedding for face recognition and clustering, in: Computer Vision and Pattern Recognition (CVPR) 2015, pp. 815–823. doi:10.1109/CVPR.2015.7298682.

Srivastava, N., Hinton, G., Krizhevsky, A., Sutskever, I., Salakhutdinov, R., 2014. Dropout: A simple way to prevent neural networks from overfitting. Journal of Machine Learning Research 15, 1929–1958.

Studholme, C., Hill, D., Hawkes, D., 1999. An overlap invariant entropy measure of 3D medical image alignment. Pattern Recognition 32, 71 – 86. doi:10.1016/S0031-3203(98)00091-0.

Tong, T., Wolz, R., Wang, Z., Gao, Q., Misawa, K., Fujiwara, M., Mori, K., Hajnal, J.V., Rueckert, D., 2015. Discriminative dictionary learning for abdominal multi-organ segmentation. Medical Image Analysis 23, 92 – 104. doi:10.1016/j.media.2015.04.015.

Vincent, P., Larochelle, H., Bengio, Y., Manzagol, P.A., 2008. Extracting and composing robust features with denoising autoencoders, in: International Conference on Machine Learning (ICML) 2008, pp. 1096–1103. doi:10.1145/1390156.1390294.

Wachinger, C., Reuter, M., Klein, T., 2017. DeepNAT: Deep convolutional neural network for segmenting neuroanatomy. NeuroImage doi:10.1016/j.neuroimage.2017.02.035.

Wang, H., Suh, J.W., Das, S.R., Pluta, J.B., Craige, C., Yushkevich, P.A., 2013. Multi-atlas segmentation with joint label fusion. IEEE Transactions on Pattern Analysis and Machine Intelligence 35, 611–623. doi:10.1109/TPAMI.2012.143.

Wang, Z., Bhatia, K.K., Glocker, B., Marvao, A., Dawes, T., Misawa, K., Mori, K., Rueckert, D., 2014. Geodesic patch-based segmentation, in: Medical Image Computing and Computer-Assisted Intervention (MICCAI) 2014, Springer International Publishing. pp. 666–673. doi:10.1007/978-3-319-10404-1_83.

Warfield, S.K., Zou, K.H., Wells, W.M., 2004. Simultaneous truth and performance level estimation (STAPLE): an algorithm for the validation of image segmentation. IEEE Transactions on Medical Imaging 23, 903–921. doi:10.1109/TMI.2004.828354.

Wolz, R., Chu, C., Misawa, K., Fujiwara, M., Mori, K., Rueckert, D., 2013. Automated abdominal multi-organ segmentation with subject-specific atlas generation. IEEE Transactions on Medical Imaging 32, 1723–1730. doi:10.1109/TMI.2013.2265805.

Wu, G., Wang, Q., Zhang, D., Nie, F., Huang, H., Shen, D., 2014. A generative probability model of joint label fusion for multi-atlas based brain segmentation. Medical Image Analysis 18, 881 – 890. doi:10.1016/j.media.2013.10.013.

Xie, L., Sedai, S., Liang, X., Compas, C.B., Wang, H., Yushkevich, P.A., Syeda-Mahmood, T., 2015. Multi-atlas label fusion with augmented atlases for fast and accurate segmentation of cardiac MR images, in: International Symposium on Biomedical Imaging (ISBI) 2015, pp. 376–379. doi:10.1109/ISBI.2015.7163891.

Xu, Z., Burke, R.P., Lee, C.P., Baucom, R.B., Poulose, B.K., Abramson, R.G., Landman, B.A., 2015. Efficient multi-atlas abdominal segmentation on clinically acquired CT with SIMPLE context learning. Medical Image Analysis 24, 18 – 27. doi:10.1016/j.media.2015.05.009.

Yang, H., Sun, J., Li, H., Wang, L., Xu, Z., 2016. Deep fusion net for multi-atlas segmentation: Application to cardiac MR images, in: Medical Image Computing and Computer-Assisted Intervention (MICCAI) 2016, Springer International Publishing. pp. 521–528. doi:10.1007/978-3-319-46723-8_60.

Zheng, Z., Zheng, L., Yang, Y., 2016. A discriminatively learned CNN embedding for person re-identification. CoRR abs/1611.05666. URL: arxiv.org/abs/1611.05666.

Zhuang, X., Shen, J., 2016. Multi-scale patch and multi-modality atlases for whole heart segmentation of MRI. Medical Image Analysis 31, 77 – 87. doi:10.1016/j.media.2016.02.006.